Sensing Atmospheric Structure: GPS Water-Vapor Tomography to Improve Severe Weather Forecasts

Final Report for FY2001 Smithsonian Astrophysical Observatory IR&D project

Investigators: Pedro Elósegui and James L. Davis

April 6, 2001

Contents

1. Introduction

The Global Positioning System (GPS) has the potential to become a significant asset for atmospheric research. The delay induced by the (neutral) atmosphere in the GPS signals can be estimated with a precision of a few milimeters from simultaneous observations to about a dozen GPS satellites. These delays can then be converted into water vapor, resulting in a continuous, accurate, all-weather, real-time GPS-derived moisture field.

Heretofore, GPS networks have demonstrated the ability to accurately determine the horizontal structure of the time-varying atmospheric water vapor. GPS atmospheric applications have largely focused on the study of mesoscale weather systems and near real-time forecasting. The vertical structure of water vapor, however, has remained largely elusive, and no one has yet demonstrated the possibility of GPS water vapor profiling under rapidly varying conditions. The extreme and rapidly changing weather experienced at Mt. Washington, New Hampshire, due in part to the vertical motions of the jet stream, makes this site unique for studying the critical role played by water vapor in atmospheric processes.

The deployment of a permanent GPS network for this purpose is a long-term and expensive effort. In this FY2001 IR&D funded project we have undertaken a very preliminary step towards this greater goal. This step consisted of conducting a small GPS experiment at Mt. Washington and evaluating the use of tomography

Figure 1. Westward-looking view of the Mt. Washington area. Yellow ellipses mark the approximate location of the GPS sites at altitudes (in meters) of: BASE, 501; DEPO, 755; FT40, 1209; FT50, 1417; and MTWN, 1888 m. Site BASE was on the roof of the Bretton Woods Hotel, site DEPO was at the MWO facilities by the cog railroad depot, sites FT40 and FT50 were along the cog railway, which is the only access from the west, and site MTWN was the FSL system at the MWO facilities on the summit of Mt. Washington. Another site (not shown) is in the town of Bartlett, 22.346 km N150°E from the summit of Mt. Washington.

for determining the three-dimensional structure of the rapidly varying time-dependent water-vapor field in this environment. In Sections 2 and 3, we describe this experiment and the analysis of the phase observations. In Sections 4–7, we present the algorithms used for tomography in the LOTTOS program, the improvements we made to this program, simulations we performed as a part of a sensitivity and resolution analysis, and our tomographic results. (The changes are presented in detail in Section 9.) In Section 8, we summarize our conclusions regarding the use of tomography to address the problem of near real-time forecasting.

2. GPS experiment

We had established working contact with staff from the Mt. Washington Observatory (MWO) in July 2000. In August 2000 we visited their headquarters in North Conway, New Hampshire, where we met with Dr. Rancourt, research head of MWO. In that initial trip, we also conducted a field reconnaissance, assisted by Dr. Rancourt. We identified a number of potential GPS sites. Of these, we chose three sites along the west side of Mt. Washington for the following reasons: (1) meteorological data recorded at the summit of Mt. Washington and provided by the MWO indicate that 70% of the Mt. Washington weather comes from the west-northwest, (2) the Mt. Washington Cog Railway runs along this side of the Mountain and would simplify equipment hauling and access to the two remote sites, (3) the forest clearing alongside the cog railroad provides excellent visibility to the GPS satellites, and (4) the GPS systems cause no environmental impact. A fourth site was to be placed at the base

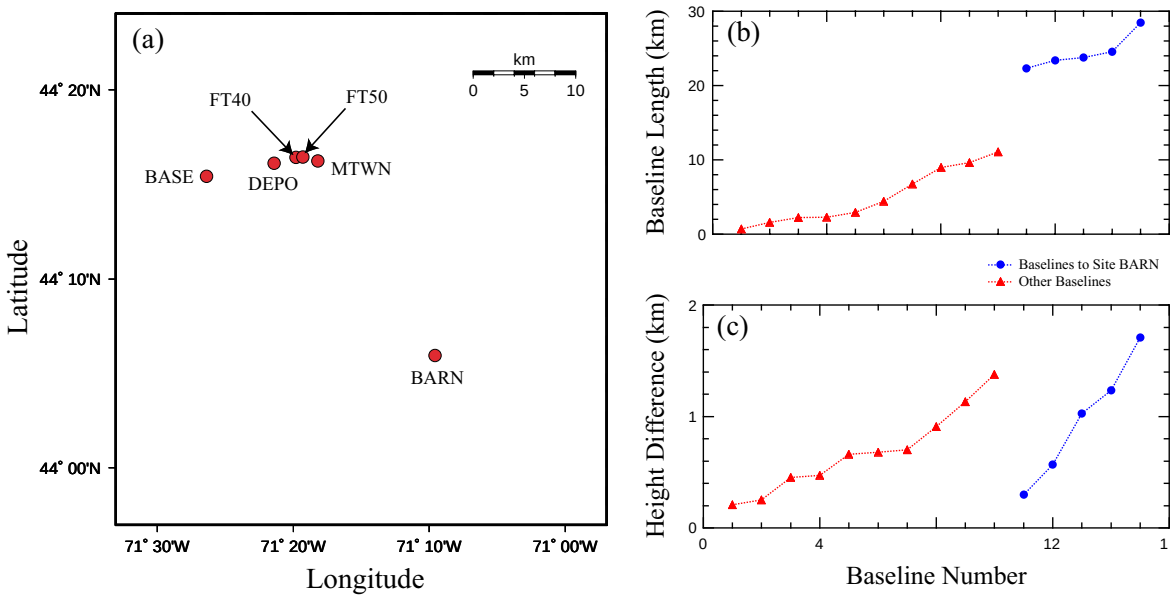

Figure 2. (a) Plan view and geographical location of the GPS network, (b) baseline lengths, and (c) baseline vertical components. Baseline numbers 11–15 are to site BARN, in Bartlett, which was not used in the tomographic inversions (see below).

of Mt. Washington at the Bretton Woods Hotel. Dr. Rancourt assisted us in coordinating with the Bretton Woods Hotel and the Mt. Washington Cog Railway. Figure 1 shows a pictorial view of Mt. Washington and the network and Figure 2 shows the network geometry. Baseline components ranged in length between 0.697–28.471 km and vertically between 0.208–1.709 km.

We established contact with Drs. Gutman and Holub from NOAA's Forecast Systems Laboratory (FSL) and with Dr. Wolfe from NOAA's Environmental Technology Laboratory (ETL), and coordinated our experiment with their installation of a GPS system on the summit of Mt. Washington. FSL has an additional GPS system operating permanently in Bartlett, New Hampshire, as part of NOAA/FSL Ground-Based GPS Integrated Precipitable Water Vapor Demonstration Network.

We used four of our own GPS systems, plus two choke-ring antennas loaned from the University Navstar Consortium (UNAVCO). We also borrowed from UNAVCO three sets of meteorological packages and four radio modems. Prior to the experiment, we thoroughly checked the equipment borrowed from UNAVCO as well as the four GPS systems that we possess at the Smithsonian Astrophysical Observatory (SAO). J. Normandeau of SAO opened and fixed a SAO faulty receiver that turned out to have a broken solder connection. Without this fix and with no time for a replacement, the experiment would have been undertaken with only three receivers.

Because of the potential for severe weather during the experiment and the remoteness of two of the sites with no access to external power, safety was an important

consideration in our planning. In order that the equipment endure the weather conditions at these sites, we used deep-cycle batteries and ruggedized the systems with tarpaulin and wires. To guarantee a safe experiment we took some specific personal measures which we will be described below.

We set up the four Trimble SSI GPS receivers with Dorne-Margolin antennas and collected data continuously during October 19–26, 2000. All the sites were located within the confines of the White Mountain National Forest. Dr. Rancourt provided access to a fenced hut with external power for one site and an insulated and ruggedized enclosure for another.

We installed a meteorological package at each of sites DEPO, FT40 and FT50 to measure pressure, temperature and relative humidity at 10 minutes intervals. Meteorological variables were also measured at the MWO facilities on the summit of Mt. Washington, were the MTWN site was located. However, no meteorological measurements were available at site BASE, on the roof of Bretton Woods Hotel.

We stayed in North Conway during the duration of the experiment in order to monitor continually the equipment and to be ready in case of failures. (None occurred.) We toured the sites daily and mounted a radio modem on our vehicles roof for routine remote equipment checks. For safety, we carried redundant mobile communication devices (two-way radios borrowed from MWO and cell phones) and checked in frequently with the MWO staff while on the mountain. We visited the remote sites only while installing and taking down the GPS systems. We visited those sites in clement weather, when the cog railway was in operation. For easy orientation, we installed the two remote sites within sight of the cog railway. The staff and operators of the cog railway were informed of our schedule for visiting and leaving the sites. Their assistance was key to the success of the experiment.

3. Analysis of the raw phase observations

The component of the neutral atmosphere in hydrostatic equilibrium, primarily nitrogen and oxygen, can be quite accurately estimated simply by measuring the barometric pressure at the surface [e.g., *Davis et al.*, 1985]. The total column density of water vapor, however, cannot be accurately sensed from surface meteorological measurements because it is very poorly mixed in the atmosphere and presents large spatial and temporal variability. At sea level in the local zenith direction, the additional delay that the signal experiences due to the hydrostatic component of the troposphere, called "hydrostatic delay," is ∼2300 mm. The corresponding nominal delay caused by the water vapor, called "wet delay," is ∼100 mm, with extreme values of about 400 mm in the tropics.

We used the GIPSY software package [*Webb and Zumberge*, 1993] and standard estimation strategies [e.g., *Elósegui et al.*, 1999] to determine values of the time-variable atmospheric-delays induced in the GPS signals by the neutral atmosphere at each site. In essence, using the data from each day (starting at 0 UTC), together with precise orbits and consistent earth-rotation parameters both obtained from the International

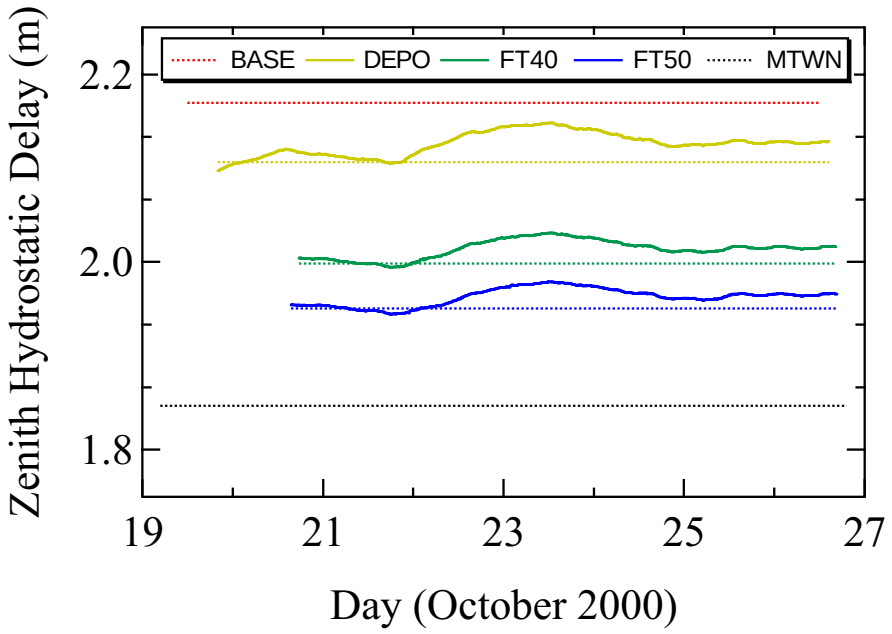

Figure 3. Zenith hydrostatic delays based on surface pressure measurements (solid line) and exponential law based on altitude above the ellipsoid (dotted line). For comparison, both estimates are shown for the three sites where surface pressure measurements were available.

GPS Service (IGS), we formed the ionosphere-free carrier phase and pseudo-range combinations and estimated the three components of position for all six sites, carrier phase ambiguities, station clocks, and atmospheric zenith delays and delay gradient parameters. From these 24 hr, eight-day independent solutions, we calculated weighted-average positions for all six sites and reprocessed the daily solutions with their three components of positions constrained to cm-level. The daily root-mean-square (RMS) postfit phase residuals from these latter solutions was typically ∼2 mm.

The atmospheric delay is modeled as the sum of a hydrostatic and a wet component [*Davis et al.*, 1993]. These delays are parameterized in terms of a zenith delay and delay-gradient parameters, each of which are mapped to the proper direction using a mapping function, assumed known. In the data analysis, we use as *a priori* estimates of the zenith delay our best estimates of the hydrostatic delay, obtained from measurements of the pressure at those sites with barometers (DEPO, FT40 and FT50) or from extrapolation of a nominal sea-level surface pressure based on the site altitude for the other sites. In the future, we need to be able to extrapolate local pressure measurements for use in GIPSY, but we did not have time to make this correction during the period of funding. The *a priori* delay-gradient parameters were taken to be zero.

GIPSY then estimates corrections to the *a priori* zenith-delay and delay-gradient parameters, which, do to our choices for *a priori* value, we take to be solely due to

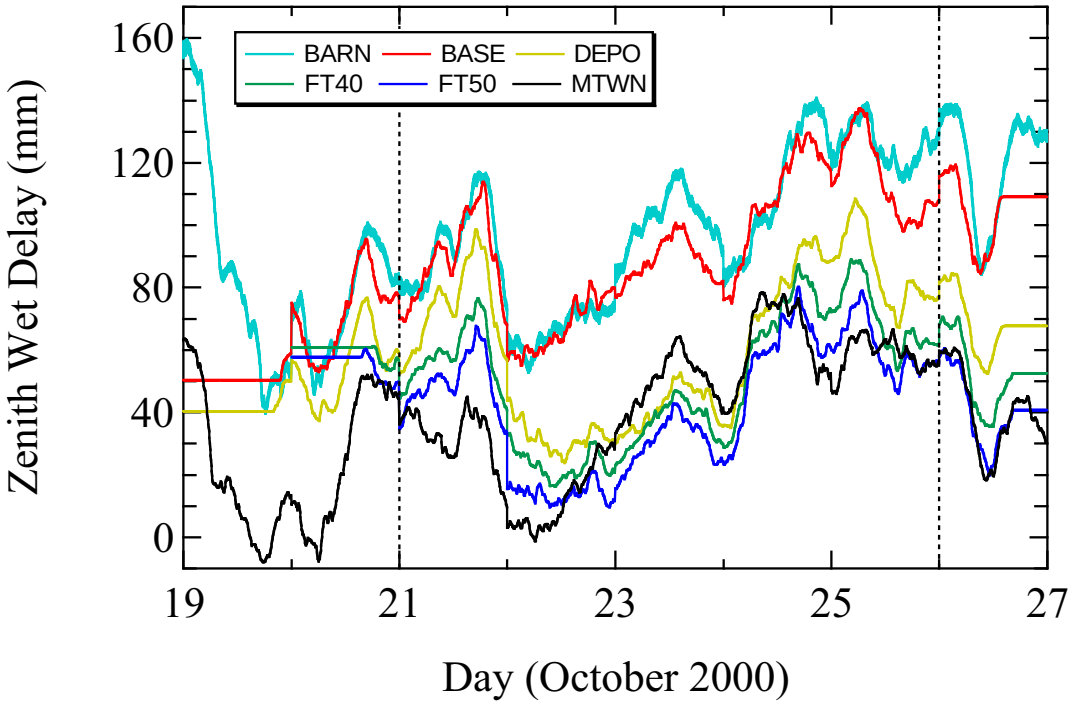

Figure 4. (a) GPS-derived estimates of zenith wet delays. For clarity, the standard deviations of the zenith wet delay estimates for site BARN only (light blue) have been plotted. These standard deviations range between 1.1 and 3.4 mm, based on the propagated measurement noise of 10 mm. Formal uncertainties for the other sites are similar to those of BARN. Tomographic analysis has been performed using data from October 21–25 (vertical dotted lines), when all sites were collecting data. Line segments of constant value represent lack of data at a particular site.

the wet atmosphere. Systematic errors therefore are possible due to: (1) Errors in the pressure measurements, which we take to be ∼0.7 mm of zenith delay; (2) Errors in the pressure extrapolation, which we calculate could be as large as ∼40 mm, with this maximum error occurring on October 23; (3) Errors in the assumption of hydrostatic equilibrium; (4) Non-zero gradients in the hydrostatic delay; and (5) Other systematic errors associated with the atmospheric delay or other contribution to the phase.

Figure 4 shows the GPS-derived estimates of zenith wet delays, which were modeled as a loosely constrained random walk process (variance rate of 9 mm^2 hr^{-1}) and its values were estimated at 300 s intervals. We used an elevation angle minimum of 7° and the *Niell* [1996] hydrostatic and wet mapping functions.

4. Tomographic algorithms used: The LOTTOS software

GPS tomography is conceptually similar to tomographic techniques used in other disciplines such as medicine and seismology. In essence, each antenna receives signals simultaneously from about a dozen GPS satellites in the field of view. The information

contained in each of these signals is in the form of integrated water-vapor. In a small-scale network of GPS receivers, multiple rays traverse the troposphere right above the network. Such network experiences multiple ray crossings as rays from different satellites to receivers intersect at various altitudes. The chance of rays crossing at altitude is further increased by also providing a vertical distribution of receivers. An inverse theory approach enables us to estimate the local atmospheric radio refractivity from the (redundant) integrated water-vapor measurements.

The integrated water-vapor measurements are expressed as

$$\tau_w \simeq \frac{10^{-6}}{c} \int_S N_w(s) ds \tag{1}$$

where c is the speed of light in vacuum, the path of integration is along the signal (ray) path S, $N = 10^6(n-1)$ is the refractivity (whose "dimensionless" units are Nepers, or equivalently mm of electrical path delay per km of geometric distance), n is the index of refraction, and the subscript w refers to water-vapor. GPS tomography consists of obtaining estimates of the water-vapor refractivity field from measurements of integrated water-vapor by inverting a discretized form of (1). To account for the temporal variations of the wet refractivity field, one such inversion is performed at each observing epoch or group of epochs during which the refractivity is assumed to remain constant.

We used the Local Tropospheric Tomography Sotfware (LOTTOS) package [*Flores*, 1999], provided by Drs. Flores and Rius of Institut d'Estudis Espacials de Catalunya (IEEC), which performs a linear inversion of integrated GPS water-vapor measurements from a given epoch to estimate refractivity at a given point and time, and propagates the system forward in time using a Kalman filter. Below, I briefly describe the functions of LOTTOS. For more details, see *Flores* [1999] and *Flores et al.* [2000].

4-1. Calculation of slant wet delays

The tomographic observable is the integrated water-vapor measurement along the GPS receiver-to-satellite line-of-sight, also known as the slant wet delay. The slant wet delay, however, is not a pure GPS observable but a quantity constructed from the parameter estimates and the data. In LOTTOS, the slant wet delay at a given epoch and for an observation in the direction of a visible satellite is constructed by mapping the estimated zenith wet delay and delay gradient parameters to each ray direction, and adding the postfit residuals phase observation:

$$\tau_w(\varepsilon, \phi) = m(\varepsilon) \left[\tau_w^z + \vec{G} \cdot \hat{\rho}(\phi) \cot \varepsilon \right] + \tau_r(\varepsilon, \phi) \tag{2}$$

In (2), ε is the elevation angle of the satellite at the receiving site and ϕ is its azimuth angle, τ_w^z is the zenith delay estimated from the GIPSY analysis, $\vec{G}$ is the delay gradient parameter also estimated from the GIPSY analysis, $\hat{\rho}$ is the unit vector representing the

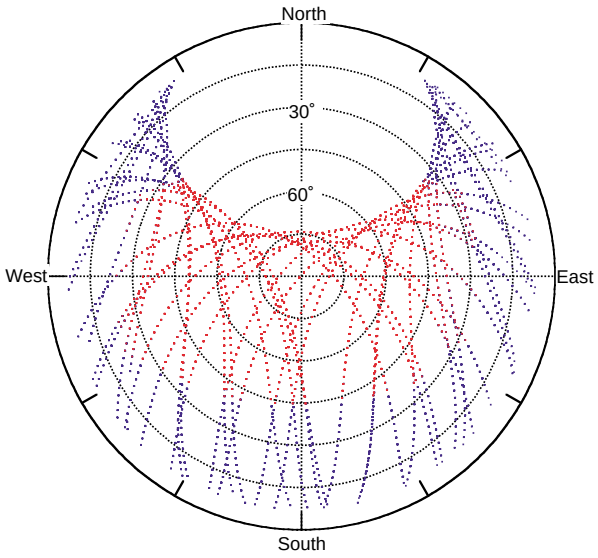

Figure 5. Direction vectors of accepted (red) and discarded (blue) rays for October 21, 2000.

horizontal projection of the site-to-satellite topocentric vector, m is the wet mapping function, and τ_r is the postfit residual from the GIPSY analysis.

There are several assumptions implicit in forming these retrieved slant delays. It is assumed the the only contributions to the atmospheric propagation delay are the hydrostatic and wet components, and that these can be separated in the GIPSY analysis. It is also assumed that postfit phase residuals can be interpreted solely in terms of slant wet delay contributions. This latter assumption will be violated in principle in any least-squares solution, and will certainly be violated given the systematic errors we believe to be present. To what degree this assumption is violated, however, has never been properly addressed in any GPS-tomography studies.

4-2. Discretization

LOTTOS discretizes the atmosphere above the network in volume cells of finite size ("voxels") and takes the wet refractivity within each volume to be constant. This discretization transforms the integral in (1) into a summation, whereby the ith wet slant delay "observable" is modeled as

$$\tau_w(i) = \sum_j a(i,j)\, N_w(j) + \epsilon_i \tag{3}$$

where $a(i,j)$ is the length of the (straight-line) ray within the voxel j multiplied by $10^{-6}/c$, $N_w(j)$ is the refractivity in this voxel, and ϵ_i is measurement error. The summation is conducted only over those voxels through which the ray travels.

The system of voxels is constructed as a three-dimensional grid above the network, with all the voxels of equal dimension. The entire set of voxels therefore forms a

"box" over the network. Many of the rays pass out of the top of the box, at which altitude and above the wet refractivity is assumed to be zero. Some low elevation-angle rays, though, pass out the sides of the box. LOTTOS handles this situation by discarding those observations for which this occurs (Figure 4). LOTTOS combines all the accepted observations from all the sites within an epoch range during which the refractivity is assumed to be constant in time. This will leave us with N observations and therefore N observation-equations that can be expressed in vector-matrix notation as

$$y = A\,x + \epsilon \tag{4}$$

where y is the vector of N reconstructed slant wet delays, x is the vector of M (unknown) parameters representing the wet refractivity in all the M voxels, A is the $N \times M$ matrix of a values, and ϵ is a vector of (unknown) measurement errors.

4-3. Constraints

The system expressed by (4) is typically underdetermined because not all individual volumes are crossed by rays. To constrain the problem, constraint equations are imposed. LOTTOS generally imposes a boundary constraint to the topmost layer of voxels, in which the wet refractivity is constrained to zero. This assumption is probably quite accurate for topmost layers at or above 10 km, as radiosonde profiles typically indicate a scale height for water vapor of ∼1–2 km. LOTTOS also imposes smoothing constraints. Originally, smoothing was imposed both horizontally and vertically (independently) using constraint equations expressing the value of the refractivity in voxel as the Gaussian-weighted average of the voxels surrounding it. Except during instances of frontal passages, the wet refractivity field over small spatial scales is probably rather smooth horizontally and a Gaussian-weighted smoothing scheme is probably adequate. Whereas this constraint form may be adequate for horizontal layers, we have found it to be less satisfactory for vertical columns, and have developed a new vertical smoothing constraint (see below).

No lateral boundary constraints can currently be applied, which may have an effect on estimates of refractivity in volumes located along lateral boundaries. To avoid possible boundary-effect errors in the solution, the horizontal area covered by the grid can be made several times larger than the area spanned by the network and then concentrate only on estimates of refractivity in volumes directly above the GPS network.

4-4. Inversion

The least-squares solution to the constrained system can be written as

$$\hat{x} = \left[A^T \Lambda_y^{-1} A + C^T W C\right]^{-1} A^T \Lambda_y^{-1} y \tag{5}$$

where Λ_y^{-1} is the measurement covariance matrix, C is the design matrix for the system of constraints, and W is a weight matrix for the constraints. Both Λ_y and W are generally taken to be diagonal, and the values for these matrices, as well as the values for several parameters required by the constraints (such as the σ parameter in the Gaussian smoothing) must be chosen by the user.

4-5. The time domain

A Kalman filter with backward smoothing is used to account for the temporal variation of the wet refractivity field, which is modeled as a random walk stochastic process. Although a random walk may be an adequate stochastic process for modeling the wet refractivity field based on the statistics of other atmospheric observables (e.g., zenith wet delay), the selection and effect of this particular process to model the refractivity field should be further investigated.

5. Improvements to the tomography software

During the course of implementation of LOTTOS and performing simulations, we found several problems that significantly effected the ability of the software to correctly calculate the best-fit refractivity parameters and their uncertainties. For example, the bugs affected the reconstruction of the slant wet delays, the choice of rays to reject, the calculation of the path lengths through the voxels, the calculation of the normal equations, and the calculation of the standard deviations of the refractivity estimates. A significant amount of time on this project has been devoted to fix these bugs and also to modify other parts of the software.

An example of other improvements made to the software includes a new vertical smoothing algorithm. The new algorithm lightly constrains the wet refractivity to be equal across layer boundary surfaces, with the weight constraints increasing exponentially with increasing altitude. This new algorithm is more in accord with data from radiosondes and other sensors, which indicate that water vapor variation decreases with altitude.

Section 9 provides a detailed description of the bugs found and changes made to the software.

6. Tomographic simulations and sensitivity analyses

We have performed several series of tomographic simulations to assess the ability to resolve the spatio-temporal variations of the refractivity field. In all our simulations, we used the actual geometry of our experiment as determined by the ground-based static locations of the five sites along the west side of Mt. Washington, the space-based time-varying location of the GPS satellite constellation, and a data sampling of one observation every 300 s. This geometry and sampling rate resulted in about a total of 9500 rays per day. Using the actual experiment geometry, we generated synthetic slant wet delays using several different wet refractivity profiles some based

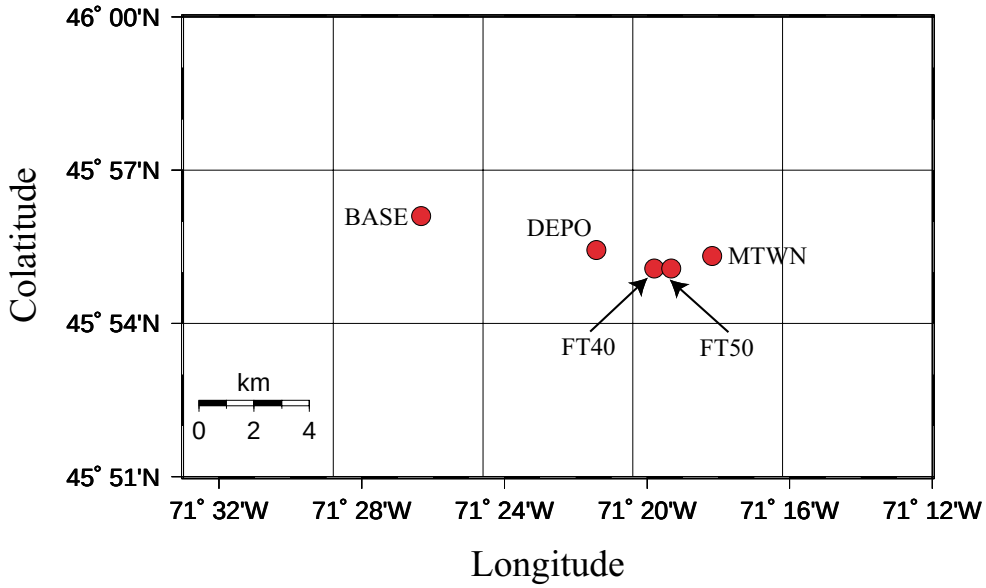

Figure 6. Plan view and geographical location of the discretization employed.

on radiosonde data. To a great extent, these simulations were used in debugging the software. However, we will present results only from the most relevant "post-debugged" simulations.

Prior to performing these simulations, we calculated the number and locations of ray crossings above the GPS network. A ray crossing was defined to occur above the network if the minimum distance between two independent rays were $\leq$ 500 m, the approximate vertical size of a voxel (see below). Not surprisingly, the vast majority of ray crossings occur among the five sites located on the west side and summit of Mt. Washington, and very few to distant site BARN. Thus, we restricted the tomographic analysis to those five sites. Moreover, the majority of ray crossings occur along the mostly east-west line defined by these sites. Thus, we expected most of our resolving capability to be along this direction and very little along the north-south direction.

Based primarily on these findings and also on some preliminary simulations, we settled for a discretization of the atmosphere above the network up to an altitude of 10 km in 25 vertical layers of 3×5 horizontal voxels each. Figure 5 shows this discretization. The resulting voxels have a height of 400 m and horizontal dimensions of approximately 5.5×5.5 km. (The effect of the discretization should be further investigated.) The particular horizontal area selected covers a geographical area of about 25×15 km. This area resulted in a total of about half of the rays per day (about 4700) passing out from the top of the 10 km altitude layer. The other half pass out from the sides (Figure 5). The number of rays that pass out from the top of the grid could be increased by enlarging the horizontal area, with a concomitant dependence on, and therefore sensitivity to, the horizontal constraints. The approximate geographical

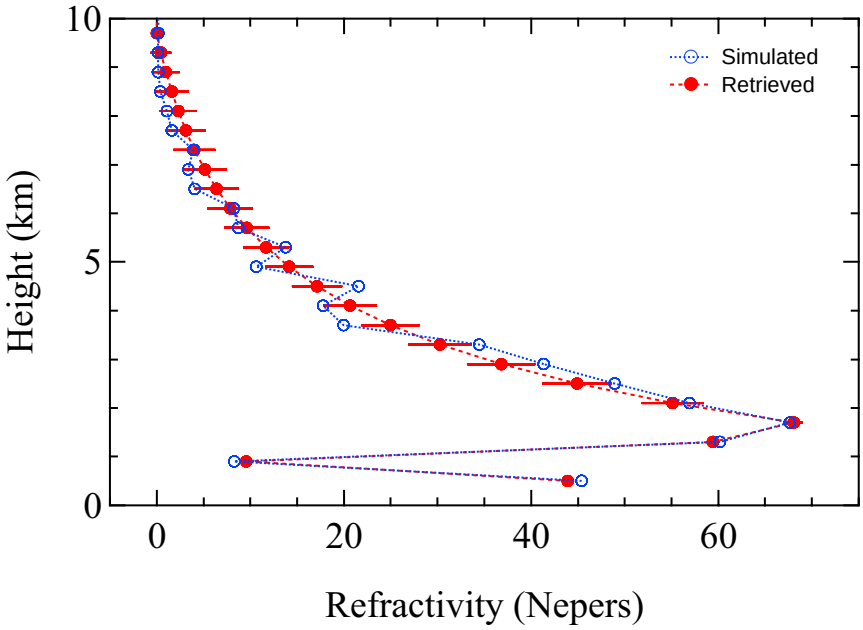

Figure 7. Simulated (blue) and retrieved (red) refractivity profile. Standard deviations are based on the propagated measurement noise of 1 mm of (wet) delay.

area required to have all possible rays down to an elevation angle of 7° included in the grid is 150 × 150 km, which is unreasonable.

In the reminder of this section, we present results from four simulations, which are shown in Figures 7–10. Figure 7 shows a retrieved refractivity profile from the ground up to a height of 10 km. The simulated profile was generated by interpolating the refractivity derived from observations from a radiosonde launched from Portland, Maine, to the altitude levels of the 25 discretized layers. The profile illustrates an atmospheric situation of large refractivity variations at low altitudes (height < 2 km) that includes an inversion layer. The refractivity above that height decreases rather smoothly reaching zero at around 8.5 km. Unless otherwise noted, this and the following figures present the profiles for the central voxel (the voxel that contains site DEPO in Figure 6). Except for possible boundary-effect errors in the solution due to lack of lateral boundary constraints (see Section 4-3), the choice of voxel is irrelevant because the synthetic profiles included no horizontal refractivity variations and, therefore, all voxels are identical. For this solution, the refractivity of the topmost layer was constrained to be zero, as can be seen from the size of the standard deviation for this layer. Also, the new vertical smoothing algorithm (see Section 5) was used. The solution is based on 2 hr worth of data (or a total of 450 rays) during which the simulated refractivity was constant. This simulation shows that we can retrieve large refractivity variations at low altitudes with high accuracy. The horizontal error bars increase significantly after 2 km indicating that we have less sensitivity. The maximum height difference between sites is 1.4 km, which may qualitatively explain the 2 km sensitivity boundary. This needs to be examined more closely.

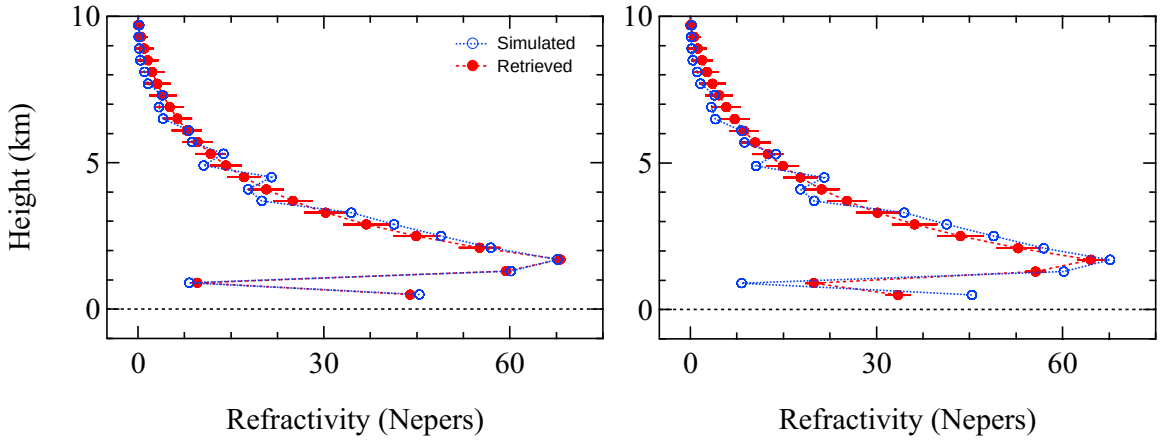

Figure 8. Retrieved refractivity (red) profile using a measurement error of 1 mm (left) and 5 mm (right) for the same simulated refractivity (blue) and parameters of Figure 7. Note that the left-hand figure is the same as Figure 7.

In Figure 8, we investigated the effect of changing the measurement errors, relative to the constant weights, on the retrieved refractivity profile. The profile in Figure 7 was obtained using a measurement error of 1 mm, which seems rather small for real observations. A more realistic measurement error for slant wet delay observations above $\sim$30° elevation angle is probably in the 5–10 mm range, though the accuracy of the reconstructed slant wet delays needs to be further investigated. As expected, the ability to resolve large refractivity variations decreases as the measurement error increases because downweighting the data also means giving more weight to the (vertical) smoothing contraints.

To further analyze the sensitivity of refractivity retrievals at high altitude, we retrieved a simulated profile that included a constant refractivity at low altitude and an inversion layer at about 5 km altitude with and without constraining the refractivity of the topmost layer to be zero. Figure 9 shows that there remains some sensitivity to refractivity variations at high altitudes. Indeed, both profiles show that while they can retrieve the refractivity at low altitudes satisfactorily the fail to retrieve the inversion layer at 5 km altitude. The most salient result from these simulations, however, is that the retrieved profile decreases to zero (within the large error bars) without having to impose such constraint and that both profiles are statistically the same.

Finally, Figure 10 serves to illustrate the improvement in retrieved refractivity profile of the new vertical smoothing algorithm implemented with respect to the original algorithm (see Section 5). The profile for the original algorithm is the best fit to the simulated profile from a range of "realistic" values of constraints tried. Whereas the new algorithm retrieves the simulated refractivity profile quite satisfactorily, the original algorithm fails to reproduce the rapid refractivity variations experienced at low altitudes. The standard deviations resulting from using the original algorithm are significantly smaller than the standard deviations from the new algorithm, which we interpret as indication that the former method unrealistically overconstrained the

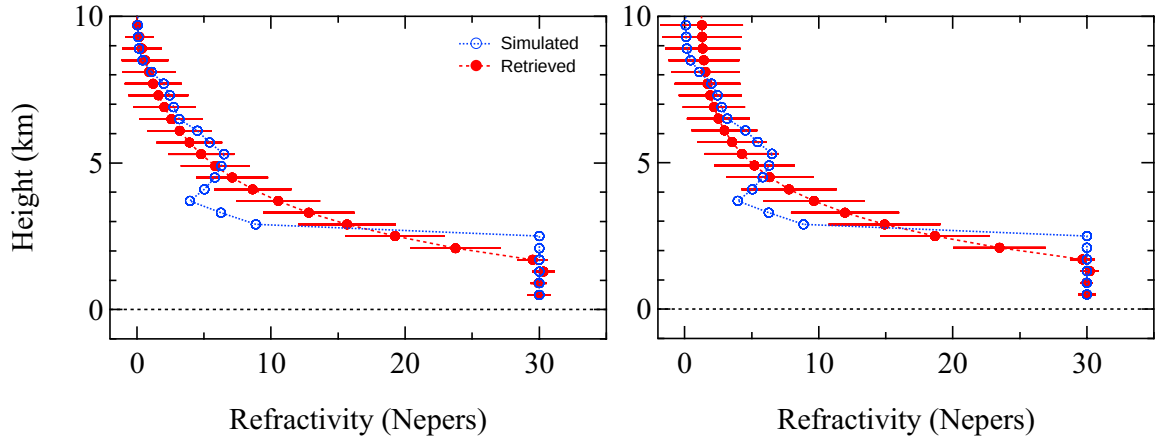

Figure 9. Simulated (blue) and retrieved refractivity (red) profile with (left) and without (right) a boundary constraint of zero refractivity for the topmost layer.

solution. Simply loosening the vertical constraints, however, did not improve the retrieved profiles. In this solution, also, the original algorithm tried to introduce spurious variations horizontally (not shown). We interpret them as not being able to separate horizontal variations from vertical variations.

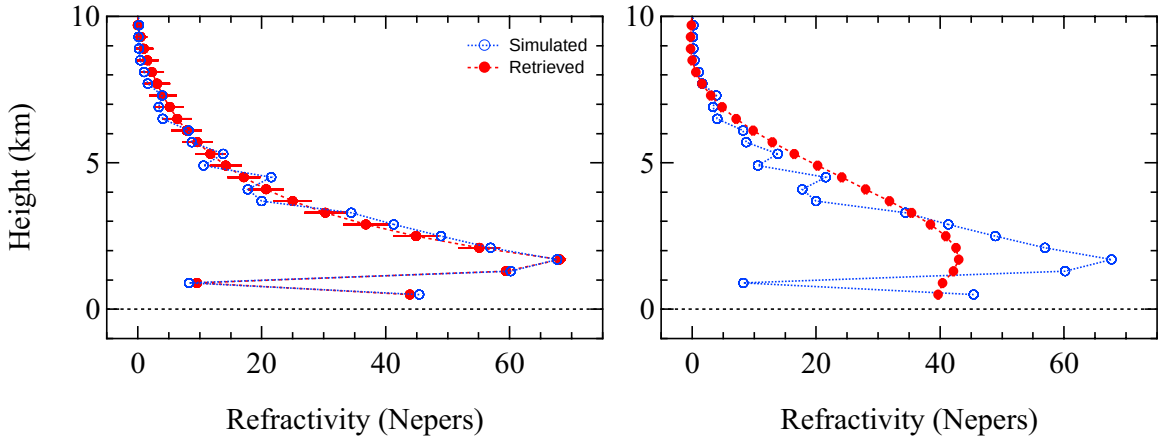

Figure 10. Retrieved refractivity (red) profile using the new (left) and the original (right) vertical smoothing algorithms for the same simulated refractivity (blue) and parameters of Figure 7. Note that the left-hand figure is the same as Figure 7.

7. Tomographic results

For each observing day between October 21–25, we constructed slant wet delays by mapping GIPSY estimates of zenith wet delay and delay gradient parameters to each ray direction as in (2). Unlike (2), we did not add the postfit residual phase observations. As explained in Section 4-1, the procedure of adding the postfit phase

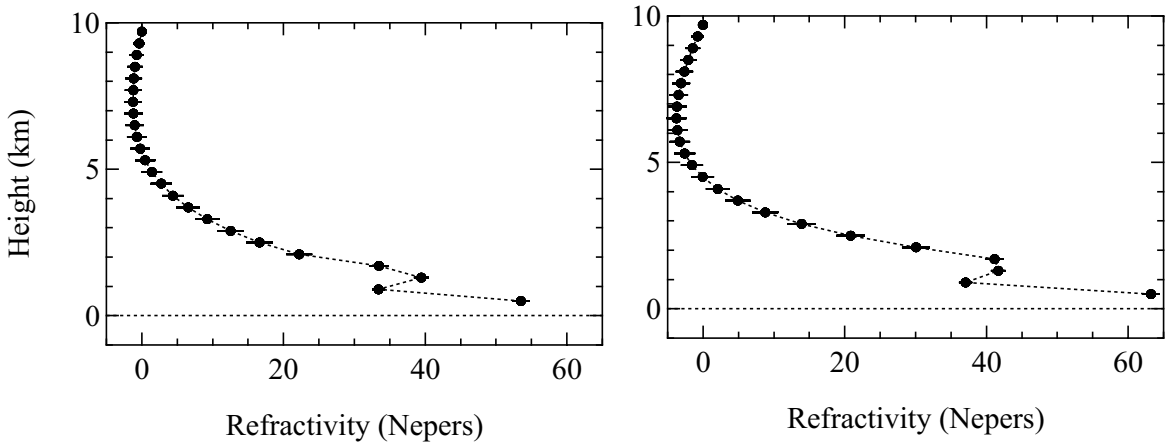

Figure 11. Examples of retrieved refractivity profiles on October 21, 2000, at 06:00–08:00 UTC (left) and 20:00–22:00 UTC (right). Standard deviations are based on the propagated measurement noise of 4 mm of (wet) delay.

residuals is inconsistent with fundamental tenets of least-square techniques. Although we consider it necessary to study the effect of adding the postfit phase residuals on the tomographic solution, we did not have the time during the period of funding.

For these 5-day, 24-hr independent data sets, we discretized the space above the network and used LOTTOS and parameters described in Section 6 to estimate the refractivity field above the GPS network. We estimated a time varying refractivity field by grouping each 24 hr data set in batches of 2 hr, and modeled the time variations of the refractivity in the Kalman filter estimator as a random walk stochastic process with variance rate of 32 Nepers^2 hr^{-1}. The selection of a 2-hr data batch represents a compromise between the total number of voxels in which the atmosphere was discretized (375) and the typical number of rays that crossed this atmospheric volume during a 2-hr period ($\sim$450). We are assuming that the wet refractivity is constant within 2 hr and that might introduce an error. The variance rate is an arbitrary, untested best guess of the level of variations of wet refractivity that one might expect based on measured variability of zenith wet delay over time periods from a few seconds to several hours. The selection and effect of these and other relevant parameters in the retrieval of the refractivity field should be further investigated. Figure 11 shows two examples of estimates of wet refractivity profile for the central voxel column. We sensed a mild inversion layer at low altitudes, where we have highest sensitivity, throughout most of October 21. The refractivity profiles remained quite similar throughout this day, with profiles tapering off to imposed zero at 10 km altitude. The profile at 20:00–22:00 UTC slightly overshoots to negative values above about 4.5 km. Negative refractivity of up to -40 Nepers where obtained on October 23. These negative values may be caused by errors in the hydrostatic delay due to errors in the assumed pressure. In fact, Figure 4 shows that on October 23 and adjacent epochs the zenith wet delay at site MTWN is larger than at sites FT50, FT40, and DEPO. This is somewhat surprising given their

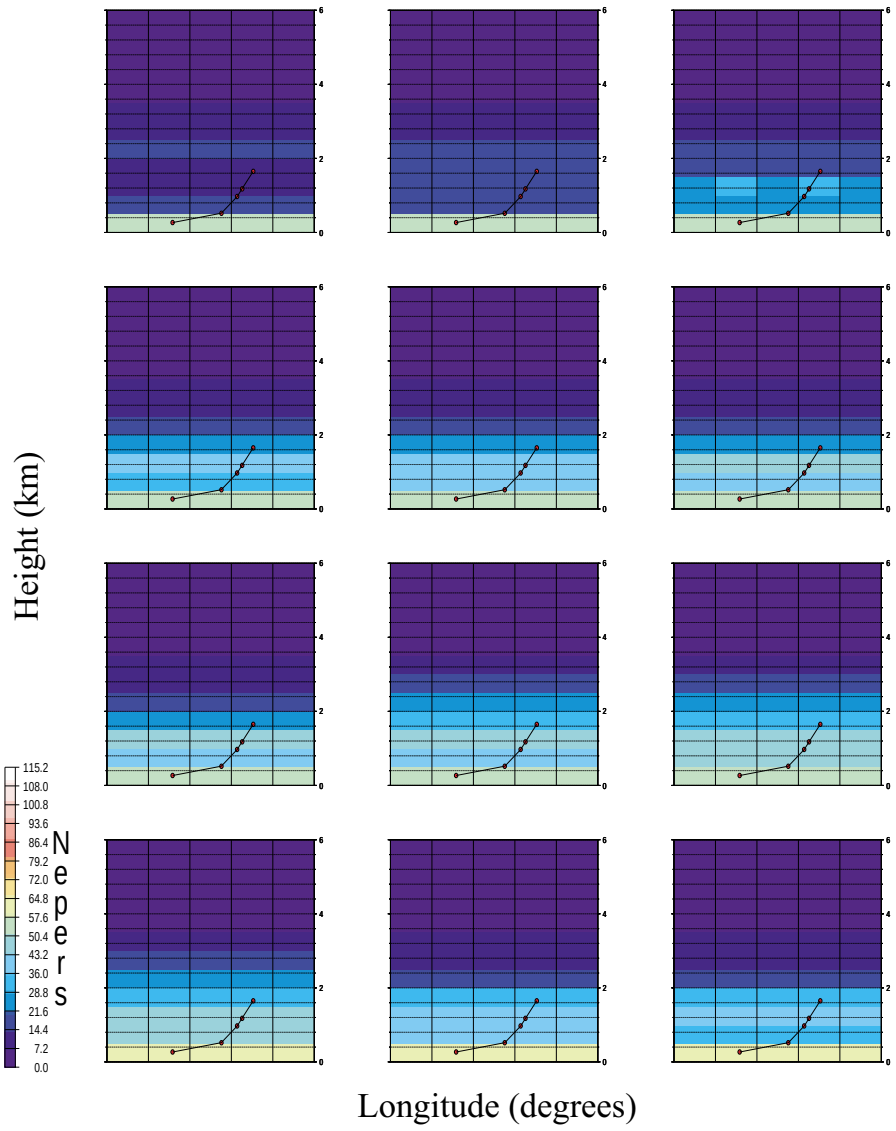

Figure 12. Estimated wet refractivity field on October 21, 2000. Each field shown is a temporal snapshot of a latitude slice along the central voxels of Figure 6, i.e., voxels with colatitude between 45°54′ and 45°57′N. Red dots are at the locations of the five GPS sites and the black thin line joining them is the simplified topography. Each temporal snapshot is the wet refractivity solution from a 2 hr data batch, starting at 00:00–02:00 UTC on the top left, and running first to the right within each row and then down along columns, to finish at 22:00–00:00 UTC on the bottom right.

altitude differences (MTWN is 471, 679, and 1133 m higher than FT50, FT40, and DEPO, respectively) and deserves further investigation.

Figure 12 shows the estimated wet refractivity field on October 21, 2000, along a longitude slice. This slice corresponds to the central latitude voxels in Figure 6. The estimated wet refractivity field in the other two longitude slices are identical to the

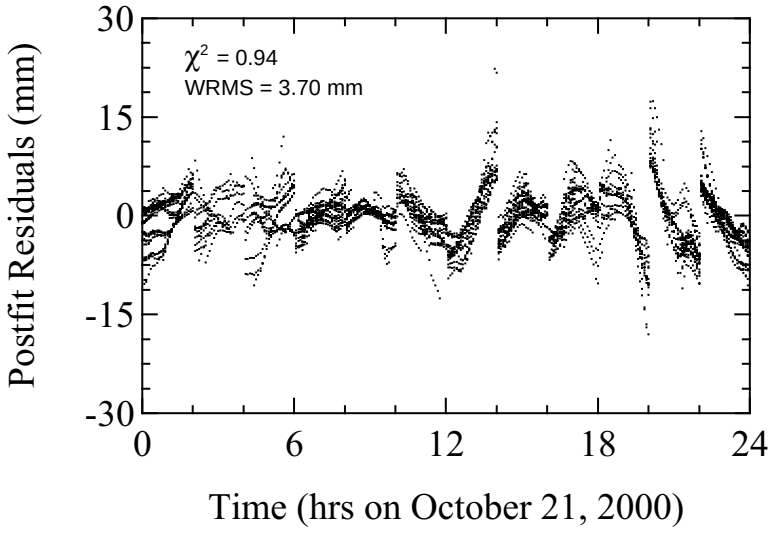

Figure 13. Postfit phase residuals on October 21, 2000. The statistics is based on a measurement noise of 4 mm of slant wet delay.

one shown. We do not seem to have any resolution to horizontal variations of wet refractivity. This may due to absence of horizontal wet refractivity variations across the network, to the horizontal smoothing constraints used, to the resolving power capability of our particular GPS network, or to a combination of them. The fact that we did not detect any horizontal variation across the network throughout the 5-day period implies that the last two are likely the reason for this lack of variability.

Figure 13 shows the postfit phase residuals on October 21, 2000. The amplitude of the residuals for the other four days were similar. The weighted (by $1/\sigma^2$) root-mean-square value of the residuals (WRMS) is 3.7 mm, and the χ^2 residual value per-degree-of-freedom (henceforth χ^2) is 0.94, and are based on a measurement noise of 4 mm of slant wet delay. The residuals present systematic trends within each 2 hr data batch, with extreme excursions of up to $\pm$20 mm. It remains to be investigated if those residuals result from assuming that the refractivity remains constant over 2 hr periods or if they are the effect of some other errors and/or assumptions.

8. Conclusions

1. Using the GPS-tomography method to analyze our data, we are most sensitive to large refractivity variations below altitudes of $\sim$2 km, measured from the lowest site in the network. The "formal" uncertainty of refractivity estimates at those height levels is $\sim$1 Neper using 2-hr time intervals. We are less sensitive to refractivity variations above 2 km. It is very encouraging that our greatest sensitivity is at altitudes where such information might be most useful.

2. The sensitivity to changes in refractivity on time scales of 2–4 hours presents the prospect of near real-time forecasting of storm events.

3. The spatial and temporal resolution that we achieved are therefore necessary, but not sufficient, for the useful applicability of GPS-tomography to the problem of rapid storm prediction on Mt. Washington. The severe weather that Mt. Washington experiences is, in part, associated with dips of the jet stream down to its summit. Since the summit is below the 2 km altitude, we do have significant spatial resolution within this region. However, we were not able to study how such storms affect, and are reflected in, changes in the wet refractivity. The likelihood of at least one storm during a 5-day period in late October is $\sim$96%, but we unfortunately did not experience any storms during the experiment.

4. Our conclusions regarding sensitivity are based on the particular geometry of our GPS network. We expect the spatial (and most likely temporal) sensitivity will improve if a denser and larger GPS network were in place. The effect of network geometry on the ability to estimate refractivity needs to be studied.

5. A number of bugs were found and corrected which influence the inferred spatio-temporal resolution of the tomographic method. We have also developed a new vertical smoothing constraint algorithm. The new algorithm reflects better the refractivity profiles and variations that are observed with other techniques. Values for tomographic parameters and methods of constraint need to be further investigated.

6. The inclusion of external observations, such as radiosonde data, needs to be considered.

7. The reason for the presence of systematic variations in the residuals of the tomographic solutions needs to be studied. These variations may result from assuming that the refractivity remains constant over 2-hr periods of time or from errors involved in the reconstruction of slant wet delay "observables," or both. Tomographic reconstructions hinge on these reconstructions and, therefore, the effect of those errors on estimates of refractivity require further study. It may also be possible to improve the time-dependence of the tomographic model by introducing rate (or higher order) parameters. The sensitivity to these model changes must be thoroughly studied.

8. We have identified a number of potential GPS sites for and have gained an understanding of the logistics for an eventual larger GPS network in the Mt. Washington area. We have also found partners that could participate in a long-term project to provide real-time GPS water-vapor tomography to improve severe weather forecast on Mt. Washington.

9. Detailed list of bugs found and corrections made

An itemized list of bugs found and other corrections and improvements made to the LOTTOS software package is presented. These changes have been fully documented in the new code version.

9-1. Bugs corrected

Routine(s)	Problem
`extract_residues.scr` `compose_residues.awk`	Residuals not converted from cm to mm.
`add_all_voxels` `gridder_simplified.F90`	Module function in recursive subroutine to generate voxel grid failed.

`cross_r`
`cross_b`
`mod_types_1d.F90`
	Crossing points of the ray with the radial and colatitudinal voxel boundaries incorrectly calculated, yielding incorrect voxel path lengths.

`prepare_constraints.F90`	Vertical constraints not restricted to proper column.
`prepare_kalman_topex.F90`	Measurement errors not squared in variance matrix.
`svdvar_dp_lt` `solve_kalman_topex.F90`	Covariance matrix from SVD algorithm reconstructed incorrectly.
`compute_solution_svd` `solve_kalman_topex.F90`	Covariance matrix scaled by incorrect chi-squared calculation.
`aty_sim` `prepare_kalman_topex.F90`	Computation of normal equations failed.

9-2. Other changes and additions made

Routine(s)	Modification
`azelcart.F90` `ray_module.F90`	Site and satellite geocenter positions from cm to mm to increase precision of calculations.
`tomographer.F90`	Calculate and report ray directions.
`simulation_field_real.F90`	Added elevation-angle weighting, add noise to observations for simulations.
`radio_profile.F90`	New program to simulate radio refractivity profile.
`prepare_aprioris.F90`	New program to generate *a priori* constraints matrix.
`prepare_constraints.F90` `solve_kalman_topex.F90`	Implement a new vertical smoothing algorithm.
`compute_solutions_svd` `solve_kalman_topex.F90`	Make the criteria for zeroing singular SVD values parameter independent.
`compute_residues.F90`	Calculate and report statistics.

10. References

Davis, J. L., Herring, T. A., Shapiro, I. I., Rogers, A. E. E., and Elgered, G., Geodesy by radio interferometry: Effects of atmospheric modeling errors on estimates of baseline length, *Radio Science*, *20*, 1593–1607, 1985.

Davis, J. L., G. Elgered, A. E. Niell, and C. E. Kuehn, Ground-based measurements of gradients in the "wet" radio refractivity of air, *Radio Science*, *28*, 1003-1018, 1993.

Elósegui, P., J. L. Davis, L. P. Gradinarsky, G. Elgered, J. M. Johansson, D. A. Tahmoush, A. Rius, Sensing atmospheric structure using small-scale space geodetic networks, *Geophysical Research Letters*, *26(16)*, 2445–2448, 1999.

Flores, A., Local tropospheric tomography software (LOTTOS) documentation, *Technical report*, *IEEC*, 1999.

Flores, A., G. Ruffini, A. Rius, 4d tropospheric tomography using GPS slant wet delays, *Ann. Geophysicae*, *18*, 223–234, 2000.

Niell, A. E., Global mapping functions for the atmosphere delay at radio wavelengths, *J. Geophys. Res.*, *101*, *NO. B2*, 3227–3246, 1996.

Webb, F.H., and J.F. Zumberge, An Introduction to the GIPSY/OASIS-II, *JPL Publ.*, *D-11088*, 1993.

11. Acknowledgments

We would like to thank Drs. Gutman, Holub, Rancourt, and Wolfe for their help with the GPS experiment. J. Normandeau oversaw the pre-experiment organization and equipment testing, and participated in site installation, monitoring, retrieval, and data download and quality check. Much of the equipment was loaned from the UNAVCO Boulder Facility. We would like to express our gratitude to Ms. B. MacPherson and Mr. N. Pelletier of the Bretton Woods Hotel for giving us permission to install one of the GPS systems in their property, and to Mr. C. Kenison and the operators of

Mt. Washington Cog Railway for permission to use the train for carrying the equipment and making special stops for loading and unloading. We are grateful to Drs. A. Flores and A. Rius for providing us with the original version of the LOTTOS software package. This work was funded by the Smithsonian Institution.